

# FOREVER22: the first bright galaxies with population III stars at redshifts $z \simeq 10 - 20$ and comparisons with JWST data

Hideobu Yajima<sup>1\*</sup>, Makito Abe<sup>1</sup>, Hajime Fukushima<sup>1</sup>, Yoshiaki Ono<sup>2</sup>, Yuichi Harikane<sup>2</sup>, Masami Ouchi<sup>2,3,4</sup>, Takuya Hashimoto<sup>5</sup>, Sadegh Khochfar<sup>6</sup>

<sup>1</sup>Center for Computational Sciences, University of Tsukuba, Ten-nodai, 1-1-1 Tsukuba, Ibaraki 305-8577, Japan

<sup>2</sup>Institute for Cosmic Ray Research, The University of Tokyo, 5-1-5 Kashiwanoha, Kashiwa, Chiba 277-8582, Japan

<sup>3</sup>Kavli IPMU (WPI), The University of Tokyo, 5-1-5 Kashiwanoha, Kashiwa, Chiba, 277-8583, Japan

<sup>4</sup>National Astronomical Observatory of Japan, 2-21-1 Osawa, Mitaka, Tokyo 181-8588, Japan

<sup>5</sup>Tomonaga Center for the History of the Universe (TCHoU), Faculty of Pure and Applied Sciences, University of Tsukuba, Tsukuba, Ibaraki 305-8571, Japan

<sup>6</sup>Institute for Astronomy, University of Edinburgh, Royal Observatory, Edinburgh, EH9 3HJ, UK

Accepted ?; Received ??; in original form ???

## ABSTRACT

We study the formation of the first galaxies in overdense regions modelled by the FORMation and EVolution of galaxies in Extremely overdense Regions motivated by SSA22 (FOREVER22) simulation project. Our simulations successfully reproduce the star formation rates and the  $M_{UV} - M_{star}$  relations of candidate galaxies at  $z \sim 10 - 14$  observed by the James Webb Space Telescope (JWST). We suggest that the observed galaxies are hosted by dark-matter haloes with  $M_h \gtrsim 10^{10} M_\odot$  and are in short-period starburst phases. On the other hand, even simulated massive galaxies in overdense regions cannot reproduce the intense star formation rates and the large stellar masses of observed candidates at  $z \sim 16$ . Also, we show that the contribution of population III stars to the UV flux decreases as the stellar mass increases and it is a few percent for galaxies with  $M_{star} \sim 10^7 M_\odot$ . Therefore, a part of the observed flux by JWST could be the light from population III stars. Our simulations suggest that the UV flux can be dominated by population III stars and the UV-slope shows  $\beta \lesssim -3$  if future observations would reach galaxies with  $M_{stars} \sim 10^5 M_\odot$  at  $z \sim 20$  of which the mass fraction of population III stars can be greater than 10 percent.

**Key words:** stars: Population III – galaxies: evolution – galaxies: formation – galaxies: high-redshift

## 1 INTRODUCTION

Understanding galaxy formation is one of the central issues in current astrophysics. In particular, the first galaxies at redshifts beyond  $z = 10$  are the most likely drivers of cosmic reionization (Yajima et al. 2009, 2011, 2014; Paardekooper et al. 2013, 2015; Wise et al. 2014; Arata et al. 2019; Ma et al. 2020; Rosdahl et al. 2022) and hosts of the first massive black holes (Regan & Haehnelt 2009; Agarwal et al. 2014; Yajima & Khochfar 2016; Wise et al. 2019; Latif et al. 2022a). Thus, revealing the formation of the first galaxies is of great importance. Using Lyman- $\alpha$  lines, a lot of galaxies at  $z \lesssim 9$  have been identified (e.g., Shibuya et al. 2012; Ono et al. 2012; Finkelstein et al. 2013; Song et al. 2016; Ouchi et al. 2018). However, the transmission of the Lyman- $\alpha$  line is reduced significantly as the neutral degree of the inter-galactic medium increases, resulting in the difficulty of galaxy observation beyond  $z \sim 10$  (Yajima et al. 2018). Recent submil-

limeter observations have successfully detected high-redshift galaxies at  $z \lesssim 9$  via the detections of [CII] 158  $\mu\text{m}$  and [OIII] 88  $\mu\text{m}$  lines (e.g., Capak et al. 2015; Inoue et al. 2016; Hashimoto et al. 2018; Tamura et al. 2019). The metal line observation is expected to be difficult if target galaxies exceed  $z \sim 10$  because of insufficient metal enrichment (e.g., Yoon et al. 2022; Bakx et al. 2022; Popping 2022). Therefore, galaxies at  $z \gtrsim 10$  have been investigated with Lyman-break technique (e.g., Oesch et al. 2013, 2016; Bouwens et al. 2019). However, the number of samples has been limited and the spectroscopic confirmations have been difficult for the sensitivities of the telescopes with a reasonable integration time.

These situations are drastically changing with observations by JWST. Using the data of the first cycle observation by JWST, high-redshift galaxies have been identified. Donnan et al. (2023) found 44 new candidate galaxies and estimated the UV luminosity functions at the redshifts  $z = 8 - 15$ . Harikane et al. (2023) found candidate galaxies at  $z \sim 16$  with large stellar masses and star formation rates (see also, Naidu et al. 2022). Furtak et al. (2023) indicated that the

\* E-mail: yajima@ccs.tsukuba.ac.jp

candidate galaxies at  $z \sim 9 - 16$  had properties of young galaxies with ages  $\sim 10 - 100$  Myr and very blue UV slope down to  $\beta \sim -3$  (see also, Topping et al. 2022; Cullen et al. 2022).

The properties of high-redshift galaxies at  $z > 6$  have been investigated in various simulation projects as CODA (Ocvirk et al. 2016), FLARES (Lovell et al. 2021), THESAN (Kannan et al. 2022b), MILLENIUMTNG (Pakmor et al. 2022), UNIVERSEMACHINE (Behroozi et al. 2019) and Santa Cruz model (Gabielpillai et al. 2022). These simulations successfully reproduced statistical properties like luminosity functions of observed galaxies at  $z \lesssim 8$ . Also, some previous works provided theoretical predictions of galaxy properties at  $z \gtrsim 10$  from the simulation results (e.g., Behroozi et al. 2020; Kannan et al. 2022a). While these simulations allow us to study the statistical natures of high-redshift galaxies with large cosmic volumes, it is still difficult to study evolution from mini-haloes hosting the population (Pop) III stars to massive galaxies due to the limited resolution.

In previous theoretical studies, galaxy formation at  $z \gtrsim 10$  proceeds with the formation of Pop III stars, the radiative feedback, and the metal enrichment via the first supernovae (e.g., Maio et al. 2011; Wise et al. 2012; Johnson et al. 2013; Smith et al. 2015; Xu et al. 2016; Chiaki & Wise 2019). Due to the metal enrichment from Pop III stars, formation sites of new Pop III stars move from higher to lower density regions in large-scale structure (e.g., Tornatore et al. 2007; Pallottini et al. 2014; Xu et al. 2016; Liu & Bromm 2020). Such numerical simulations bridging from population III stars in mini-haloes to first galaxies are still challenging. Jeon & Bromm (2019) investigated the formation of first galaxies with the halo mass of  $M_h \sim 10^9 M_\odot$  at  $z = 9$  and showed their observational properties. Abe et al. (2021) studied the impact of the initial mass function of population III stars on the physical properties of first galaxies with  $M_h \sim 10^{8-9} M_\odot$ . They showed that inducing frequent pair-instability supernovae suppress the gas mass fraction and the star formation rates (SFRs) of the first galaxies significantly for the top-heavy initial mass function. The simulated halo masses in previous works have been limited to  $\sim 10^9 M_\odot$ . Therefore, the emergent UV fluxes were too faint for the sensitivities of current telescopes.

Considering the brightness of observed candidates at  $z \gtrsim 10$ , they can be hosted in massive haloes which likely form in overdense regions. In this work, we investigate galaxy formation in overdense regions in which the halo mass exceeds  $10^{11} M_\odot$  at  $z \sim 10$ . To study the transition from population III to II stars, our simulations resolve mini-haloes and follow their growth up to the massive haloes.

Our paper is organized as follows. Section 2 shows our methodology and the information about the simulation setup. In section 3, we show the star formation histories and compare them with the observational data by JWST. Also, we study the mass fraction of Pop III stars with regard to the total stellar mass. Finally, we summarize our results and discuss the limitations of our study in section 4.

## 2 METHODOLOGY

We use the results of our simulation project FOREVER22 (Yajima et al. 2022) which focuses on protocluster regions in

the cosmic volume of  $(714 \text{ cMpc})^3$ . In this project, we use the GADGET-3 code (Springel 2005) with sub-grid models developed in the OWLS project (Schaye et al. 2010) and the FIBY project (Johnson et al. 2013). Besides, we newly updated the code by adding the photo-ionization feedback, the radiation pressure on dust, dust growth/destruction, black hole growth, and its feedback (see more, Yajima et al. 2022). The project consists of zoom-in simulations with three different levels of the mass resolution and the size of zoom-in regions: PCR (Proto-Cluster Region;  $V = (28.6 \text{ cMpc})^3$ , SPH particle mass,  $m_{\text{SPH}} = 4.1 \times 10^6 M_\odot$  and final redshift,  $z_{\text{end}} = 2.0$ ), BCG (Brightest proto-Cluster Galaxy;  $V \sim (10 \text{ cMpc})^3$ ,  $m_{\text{SPH}} = 5.0 \times 10^5 M_\odot$  and  $z_{\text{end}} = 4.0$ ), and First ( $V \sim (3 \text{ cMpc})^3$ ,  $m_{\text{SPH}} = 7.9 \times 10^3 M_\odot$  and  $z_{\text{end}} = 9.5$ ). The PCR runs reproduce the observed star formation rate densities of protoclusters at  $z \sim 2 - 6$ . Also, we confirmed that the mean density fields reproduced the observed stellar mass functions, main sequences of star formation, gas fractions, and metallicities of galaxies as a function of stellar mass well (Yajima et al. 2022). In this work, we use First runs (First0 and First1 runs) in which the most massive halo reaches  $M_h = 4.8 \times 10^{11} M_\odot$  at  $z = 9.5$ . The cosmological parameters are still under debate (Komatsu et al. 2011; Planck Collaboration et al. 2020; Freedman 2021). Considering the changing history of the parameter and Hubble parameter tension (Freedman 2021), we adopt the cosmological parameters as  $\Omega_M = 0.3, \Omega_b = 0.045, \Omega_\Lambda = 0.7, \sigma_8 = 0.82$  and  $h = 0.7$ .

In this work, we consider both Pop II and III stars. If the metallicity is lower than a critical value, the initial mass function (IMF) is likely to be a top-heavy (e.g, Chon et al. 2021). Besides, the effective temperature of Pop III stars is high  $T \sim 10^5 \text{ K}$  (Schaerer 2002). Therefore, Pop III stars can be strong sources of radiative and supernova (SN) feedback. We set the critical gas metallicity  $Z = 1.5 \times 10^{-4} Z_\odot$  below which Pop III stars form (Omukai et al. 2005; Frebel et al. 2007; Chon et al. 2021). Although the critical metallicity is still under debate, Abe et al. (2021) suggested that the physical properties of the first galaxies did not depend on it sensitively (see also, Maio et al. 2010). We assume that the IMF of Pop III stars is  $dn \propto M^{-2.35} dM$  with the mass range  $21 - 500 M_\odot$  while that of Pop II is Chabrier IMF with the range  $0.1 - 100 M_\odot$ . Because of the expensive calculation costs for the first-star formation with radiative and magnetic feedback, the IMF of Pop III stars is still under debate (Stacy & Bromm 2014; Susa et al. 2014; Hirano et al. 2015; Sugimura et al. 2020; Wollenberg et al. 2020; Latif et al. 2022b). Therefore, we adopt a simple power-law function for the IMF of Pop III stars.

In evaluating the star formation rate, we consider the star formation model based on the observed Kennicutt-Schmidt law which was developed in Schaye & Dalla Vecchia (2008). The local SFR is measured as  $\dot{m}_{\text{star}} \propto m_{\text{gas}} A (1 M_\odot \text{ pc}^{-2})^{-n} (\frac{\gamma}{G} f_g P)^{(n-1)/2}$ , where  $m_{\text{gas}}$  is the mass of a gas particle,  $\gamma = 5/3$  is the ratio of specific heats,  $f_g$  is the gas mass fraction in the galactic disc, and  $P$  is the total ISM pressure. Here, we set  $A = 1.5 \times 10^{-4} M_\odot \text{ yr}^{-1} \text{ kpc}^{-2}$  and  $\gamma = 1.4$  for  $n_H < 10^3 \text{ cm}^{-3}$  and  $\gamma = 2.0$  for  $n_H \geq 10^3 \text{ cm}^{-3}$ . The star formation model is the same as in EAGLE simulation project (Schaye et al. 2015). Star formation occurs if local gas density exceeds  $n_H = n_0 \text{ cm}^{-3} (\frac{Z}{0.002})^{-0.64}$ ,

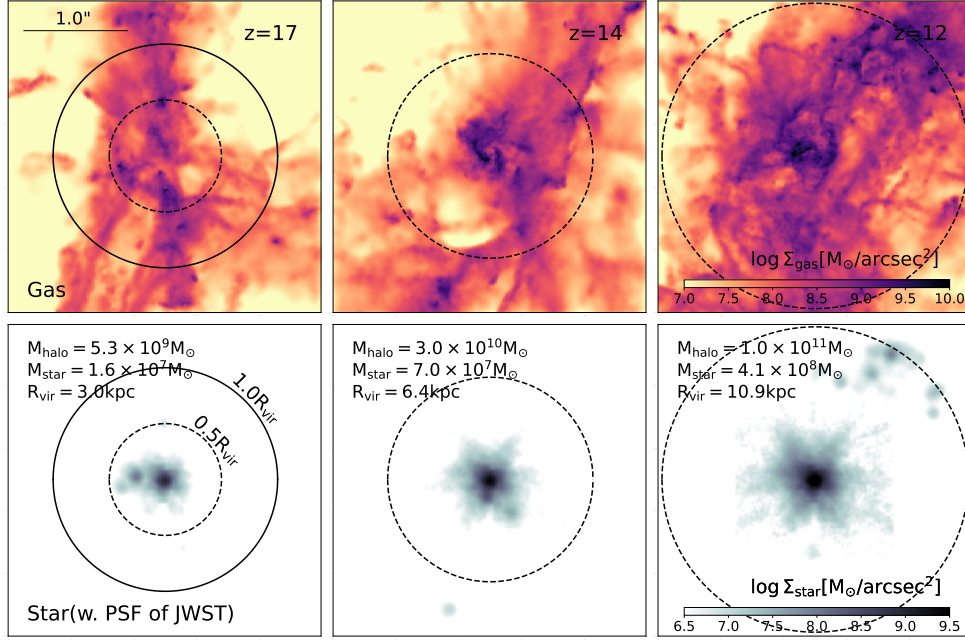


**Figure 1.** Column density maps of gas and stars in the most massive progenitors at  $z = 12, 14$  and  $17$ . The stellar distributions are smoothed with the point spread function of JWST. Halo (stellar) masses are  $5.3 \times 10^9$  ( $1.6 \times 10^7$ )  $M_\odot$  at  $z = 17$ ,  $3.0 \times 10^{10}$  ( $7.0 \times 10^7$ )  $M_\odot$  at  $z = 14$ , and  $1.0 \times 10^{11}$  ( $4.1 \times 10^8$ )  $M_\odot$  at  $z = 12$ . Solid and dashed circles represent virial radii and half virial radii, respectively. The size of the boxes is 3 arcsec, corresponding to  $L = 11.0, 9.8$  and  $8.4$  physical kpc at  $z = 12, 14$  and  $17$ .

where we set  $n_0 = 10.0$  for First runs. In the estimation of the net cooling rate, we follow the non-equilibrium chemistry of primordial gas and the equilibrium state of metals from pre-calculated tables with CLOUDY v07.02 code (Ferland 2000).

Once massive stars form, they give UV radiation feedback to surrounding gas within their lifetime  $\sim 10^7$  yr. We take into account the photo-ionization process of hydrogen and the dissociation of hydrogen molecules. We estimate the volume of the ionized region by taking the balance between the photon production rate and the total recombination rate as (see the detail, Abe et al. 2021; Yajima et al. 2022)

$$\dot{N}_{\text{ion}} = \sum_{i=1}^n \alpha_B n_{\text{HII}}^i n_e^i \frac{m_{\text{gas}}^i}{\rho_{\text{gas}}^i}, \quad (1)$$

where  $\dot{N}_{\text{ion}}$  is the photon production rate of a stellar particle,  $\alpha_B$  is the case-B recombination coefficient,  $n_{\text{HII}}^i$  and  $n_e^i$  are the ionized hydrogen and electron number densities of  $i$ -th SPH particle. In the ionized regions, the gas temperature is heated up to  $3 \times 10^4$  K, and star formation is prohibited. The dissociation rate of hydrogen molecules is evaluated based on the contributions of stars in the calculation box. First, we measure UV fluxes from stars with distances to a target gas particle as

$$J_{\text{LW},21} = \sum_{i=1}^n f_{\text{LW}} \left( \frac{r_i}{1 \text{ kpc}} \right)^{-2} \left( \frac{m_{*,i}}{10^3 M_\odot} \right), \quad (2)$$

where  $J_{\text{LW},21}$  is described in unit of  $10^{-21} \text{ erg s}^{-1} \text{ cm}^{-2} \text{ Hz}^{-1} \text{ str}^{-1}$ ,  $r_i$  is the distance from  $i$ -th stellar particle to a target gas particle and  $m_{*,i}$  is the mass of  $i$ -th stellar particle. Then, we take into account the self-shielding effect with the local  $\text{H}_2$  density and Jeans

length (Johnson et al. 2013):

$$N_{\text{H}_2} = 2 \times 10^{15} \text{ cm}^{-2} \left( \frac{f_{\text{H}_2}}{10^{-6}} \right) \left( \frac{n_{\text{H}}}{10 \text{ cm}^{-3}} \right)^{1/2} \left( \frac{T}{10^3 \text{ K}} \right)^{1/2}, \quad (3)$$

where  $f_{\text{H}_2}$  is the fraction of  $\text{H}_2$ ,  $n_{\text{H}}$  is the hydrogen number density. We consider the shielding factor derived in Wolcott-Green et al. (2011) as

$$f_{\text{shield}}(N_{\text{H}_2}, T) = \frac{0.965}{(1+x/b_5)^{1.1}} + \frac{0.035}{(1+x)^{0.5}} \times \exp[-8.5 \times 10^{-4} (1+x)^{0.5}], \quad (4)$$

where  $x \equiv N_{\text{H}_2}/5 \times 10^{14} \text{ cm}^{-2}$  and  $b_5 \equiv b/10^5 \text{ cm s}^{-1}$ . Here  $b$  is the Doppler broadening parameter,  $b \equiv (k_{\text{B}}T/m_{\text{H}})^{1/2}$ . Thus, we estimate the  $\text{H}_2$  dissociation rate ( $\kappa_{\text{diss}}$ ) by combining  $J_{\text{LW},21}$  and  $f_{\text{shield}}$  as  $\kappa_{\text{diss}} \propto f_{\text{shield}} J_{\text{LW},21}$ . In addition, we consider the photodetachment process of  $\text{H}^-$  (Shang et al. 2010). With the dissociation and formation rates, we evaluate  $\text{H}_2$  abundance and its radiative cooling rate which is a main factor in controlling the formation of Pop III stars in mini-haloes.

When the age of a stellar particle reaches  $10^7$  yr, supernova (SN) feedback turns on. Following the SN feedback model in Dalla Vecchia & Schaye (2012), we stochastically select a neighbouring gas particle and heat the temperature up to  $10^{7.5}$  K. This hot bubble rapidly expands and induces galactic wind, resulting in the suppression of star formation.

### 3 RESULTS

Figure 1 shows the column density maps of gas and stars. Stellar distributions are smoothed with a point spread func-

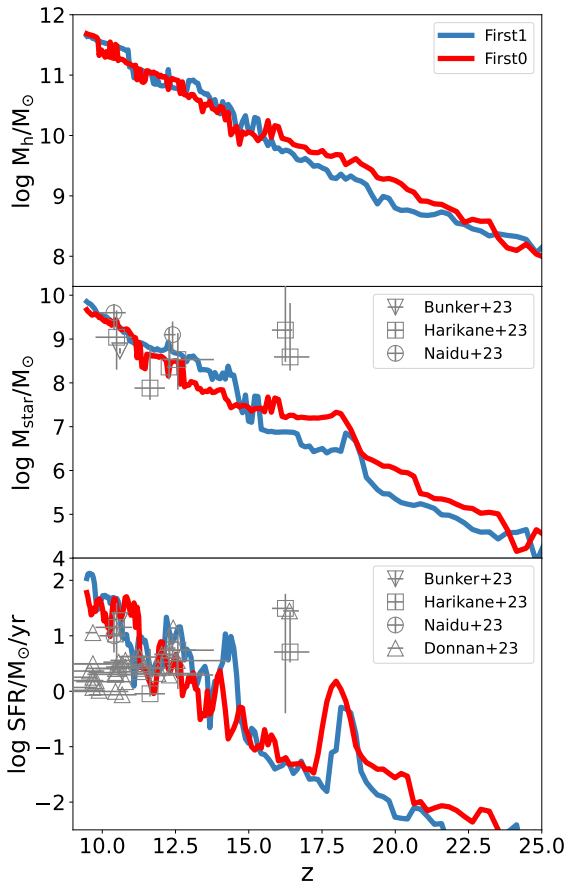


**Figure 2.** Redshift evolution of the halo, stellar mass, and star formation rate. The red and blue lines represent the properties of the most massive progenitors in First0 and First1 runs, respectively. Open symbols show the observations: inverted triangles (Jiang et al. 2021), squares (Harikane et al. 2023), circles (Naidu et al. 2022), and triangles (Donnan et al. 2023).

tion of JWST. The gas widely distributes within virial radii, while stellar distributions are compact and concentrated at the galactic centres. The gas accretes onto galaxies along the filamentary structures and the stellar feedback disturbs the gas structure. Stellar distributions and sizes change with time. At  $z = 12$ , stellar clumps distribute at  $0.5 R_{\text{vir}}$ , which reflects the minor merger phase. As the galaxy grows via baryon accretion, the size of the stellar components increases, but becomes small rapidly when major mergers happen (see also, Ono et al. 2022). Note that the size shrinkage after the merger process sensitively depends on the gas fraction and the structure of progenitor galaxies (e.g., Dekel & Cox 2006).

Figure 2 presents the redshift evolution of halo, stellar masses, and SFR. The halo masses of the main progenitors are  $\sim 10^9 M_{\odot}$  at  $z \sim 20$  and evolve to  $\sim 10^{11.5} M_{\odot}$  at  $z \sim 10$ . The fluctuations are due to mergers and the ability of the FOF group finder to identify all member particles. The rarity of the halo with  $10^{11.5} M_{\odot}$  at  $z = 10$  is

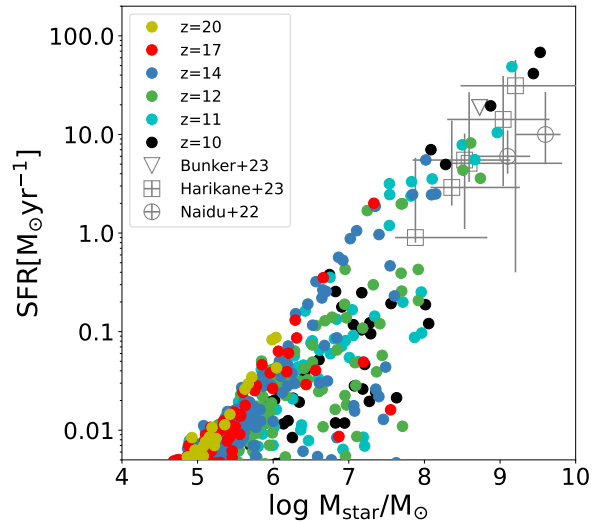


**Figure 3.** Star formation rates as a function of stellar mass. Filled circles are our simulation results. Different colors represent the different redshifts. Open symbols show the observational data: squares (Harikane et al. 2023), circles (Naidu et al. 2022) and pentagons (Bunker et al. 2023).

$dN/d\ln M_h \sim 2 \times 10^{-7} \text{ cMpc}^{-3}$ . The cosmic volume to host such a massive halo in our simulations is  $\sim 500 \text{ cMpc}^3$  that is similar to the volumes of photometric galaxy surveys with JWST (e.g., Finkelstein et al. 2023). Therefore, it can be reasonable to directly compare our simulations with JWST data. Note that, the rarity changes with time even for the most massive progenitors in the same region because of the variety of the halo merger history.

As the halo grows, the stellar mass increases. The stellar masses of the main progenitors exceed  $10^8 M_{\odot}$  at  $z \sim 13(14)$  and finally reach  $4.3(6.8) \times 10^9 M_{\odot}$  in First0 (First1) run. The stellar masses are similar to observed galaxies at  $z \lesssim 12$ . On the other hand, it is much lower than the observed ones at  $z \sim 16$ . Suppose the estimated stellar masses of observed candidates are accurate and the redshifts are actually  $\sim 16$ . In that case, most gas is very efficiently converted into stars even in the early Universe (Harikane et al. 2023). Inayoshi et al. (2022) suggested that 0.1 – 0.3 of the gas should be converted into stars by using the abundance matching technique with the observed UV luminosity functions. In our simulations, the SN feedback efficiently works in the suppression of star formation. As a result, the gas is gradually converted into stars, and the star formation efficiency ( $M_{\text{star}}/M_{\text{gas}}$ ) of main progenitors in First0 run is  $1.1 \times 10^{-1}$ ,  $2.0 \times 10^{-2}$  and  $2.5 \times 10^{-2}$  at  $z = 10, 14$  and  $17$ . Note that, the redshifts and the physical properties of the candidate galaxies at  $z > 14$  were estimated with the photometric data. It is difficult to evaluate the impacts of emission lines only from the photometric data (e.g., Schaerer & de Barros 2009). Therefore, their properties can be changed with follow-up spectroscopy (e.g., Arrabal Haro et al. 2023).

The SFR also increases with the growth of halo mass. Because of the cycle of suppression of star formation and the short recovery time scale of gas, the SFR fluctuates sig-

nificantly with time (Yajima et al. 2017). Main progenitor galaxies can have  $\gtrsim 10 M_{\odot} \text{ yr}^{-1}$  at  $z \lesssim 14$  and show starbursts with  $\text{SFR} = 50.4 (133.5) M_{\odot} \text{ yr}^{-1}$  at  $z = 9.5$  in First0 (First1) run. If we consider the star formation rate as  $\text{SFR} = \epsilon \frac{M_{\text{gas}}}{\tau_{\text{dyn}}}$  where  $\epsilon$  is an efficiency parameter and  $\tau_{\text{dyn}}$  is the dynamical time, the starbursts at  $z \sim 9.5$  correspond to  $\epsilon \sim 0.08 - 0.25$ . This value is much larger than typical star-forming galaxies in the local Universe. In the last period of 0.1 Gyr ( $z = 9.5 - 11.5$ ), the halo mass of the main progenitors in First0 run increases from  $1.2 \times 10^{11} M_{\odot}$  to  $4.8 \times 10^{11} M_{\odot}$ . The rapid mass growth with major mergers can induce the starburst. The SFRs at  $z \lesssim 14$  nicely match with the observed ones by JWST (Donnan et al. 2023; Naidu et al. 2022; Harikane et al. 2023) and GN-z11 at  $z = 10.957$  (Jiang et al. 2021). Also, the modeled galaxies reproduce the observed  $M_{\text{UV}}$  at those redshifts. As suggested in Yajima et al. (2017), once the halo mass exceeds  $10^{11} M_{\odot}$ , most gas can be trapped in the deep gravitational potential against SN feedback. This can induce the starburst with  $\text{SFR} \gtrsim 10 M_{\odot} \text{ yr}^{-1}$  and make galaxies observable. In the redshift range, black holes are still in the state of being initial seeds with  $\sim 10^5 M_{\odot}$  and the accretion rates are mostly much lower than the Eddington limit. Therefore, AGN feedback is negligible.

Figure 3 presents SFRs as a function of stellar mass. The SFR increases with the stellar mass. At  $M_{\text{star}} \lesssim 10^8 M_{\odot}$ , the suppression of SFR due to the feedback makes the large dispersion. On the other hand, massive galaxies keep the star formation continuously. We confirm that our results match the observed galaxies. The stellar mass monotonically increases with the halo mass although there is a large dispersion. The ratios of stellar to halo mass are  $\sim 10^{-3}$  and  $\sim 10^{-2}$  for  $M_{\text{h}} = 10^{10}$  and  $10^{11} M_{\odot}$  at  $z = 10$ . These values are similar to the empirical models in UNIVERSEMACHINE project Behroozi et al. (2020), while it is somewhat higher than MILLENIUMTNG (Kannan et al. 2022a). The conversion efficiency sensitively depends on the resolution, the star formation, and the feedback models. In particular, our simulations can resolve mini-haloes and dwarf galaxies, and their star formation. At high redshifts, stars formed in dwarf galaxies can contribute to the stellar mass in more massive galaxies via frequent merger processes.

We present the relationships between the UV flux  $M_{\text{UV}}$  and the halo and the stellar mass in Figure 4. We estimate  $M_{\text{UV}}$  by measuring the mean UV flux densities at  $\lambda = 1500 - 2000 \text{ \AA}$  in modelled SEDs which will be shown in Figure 6.  $M_{\text{UV}}$  is tightly related to the SFR although it somewhat changes depending on the star formation history. As the halo mass increases, the SFR becomes higher, resulting in the formation of bright galaxies. We find that the brightness can exceed the observable level  $M_{\text{UV}} \lesssim -18 \text{ mag}$  if the halo mass is larger than  $\sim 10^{10} M_{\odot}$ . In low-mass haloes, galaxies at higher redshifts form stars more efficiently because they are compact and have higher gas density typically. Also, there is a large dispersion. This can be due to the SN feedback that induces the intermittent star formation history via the cycle of gas inflow and outflow (Yajima et al. 2017). On the other hand, the UV brightness is more tightly correlated with the stellar mass. Our simulations reproduce the observed UV brightnesses nicely. Galaxies with  $M_{\text{star}} \gtrsim 10^8 M_{\odot}$  are likely to have observable UV brightness  $M_{\text{UV}} \lesssim -18 \text{ mag}$ . As shown in Figure 2, the SFR rapidly increases as the halo mass in-

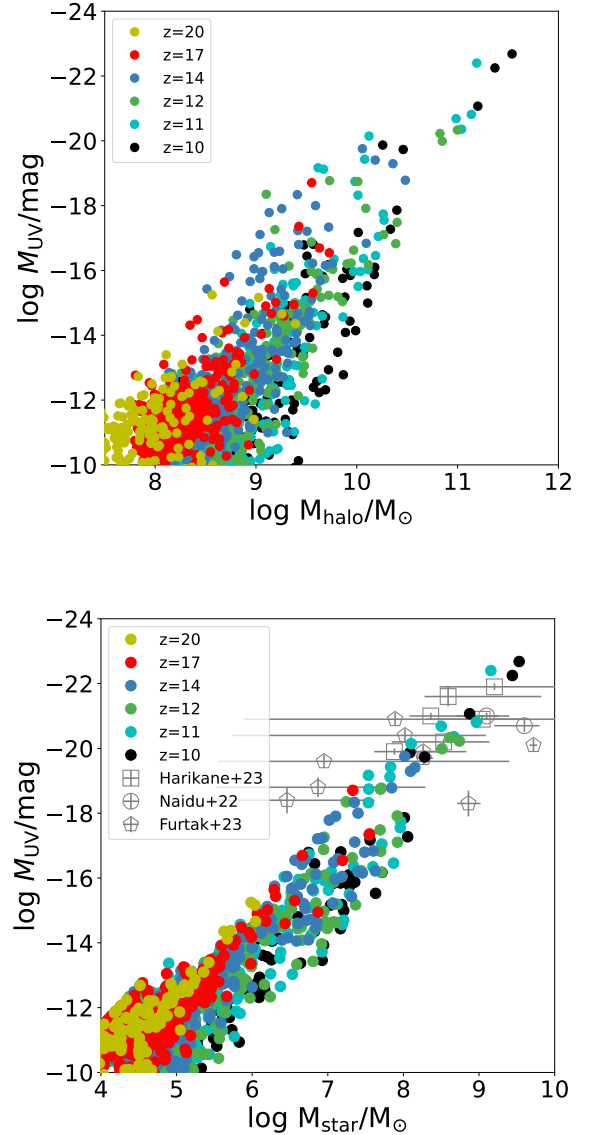


**Figure 4.** UV fluxes as a function of halo and stellar masses. Filled circles are our simulation results. Different colors represent the different redshifts. Open symbols show the observational data: squares (Harikane et al. 2023), circles (Naidu et al. 2022) and pentagons (Furtak et al. 2023).

creases. Therefore, the stellar masses in the massive haloes can be contributed mainly by the current starburst episode, resulting in the tight relation in the massive systems. Note that some observed galaxies with  $M_{\text{star}} \sim 10^{6-7} M_{\odot}$  are brighter than our modelled galaxies although they are within the error bars. As one possibility, hidden faint AGNs might contribute to observed UV fluxes (e.g., Bunker et al. 2023). Future deep spectroscopic studies will allow us to investigate AGN activities.

An upper panel of figure 5 shows the mass fraction of young population III stars to the total stellar mass. As the star formation proceeds, the interstellar gas is metal-enriched via type-II supernovae. Therefore, the fraction steeply decreases

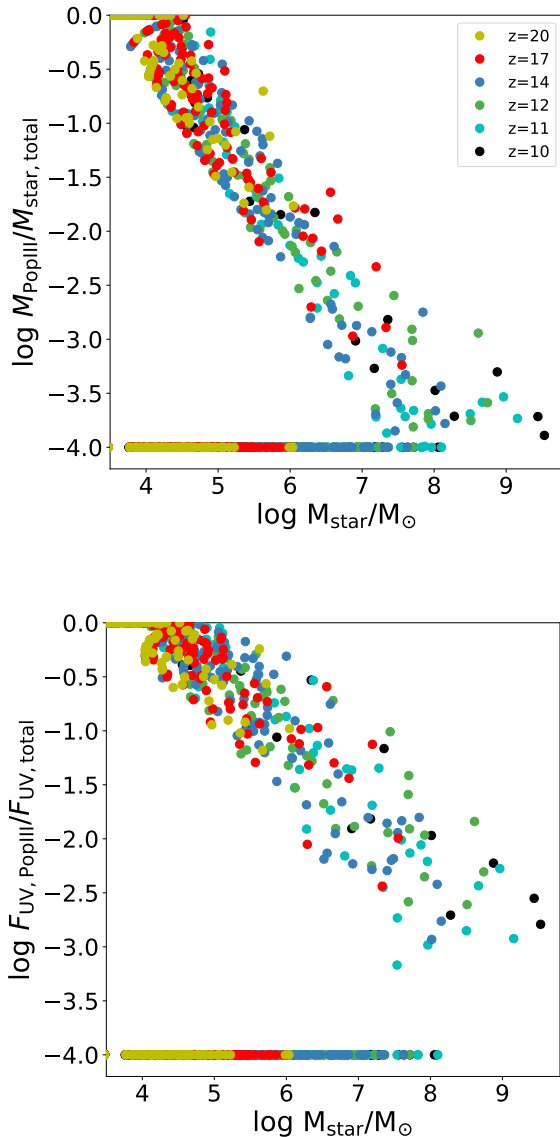


**Figure 5.** Mass fraction of young population III stars to the total stellar mass (upper panel) and their contribution fraction to UV flux at  $\lambda = 1500 \text{ \AA}$  in the rest frame (lower panel). Different colors represent the different redshifts. The galaxies with mass fractions lower than  $10^{-4}$  are plotted at  $-4.0$ .

as the stellar mass increases. Also, some fractions of galaxies have no young Pop III stars. This indicates Pop III stars form only when primordial gas clouds accrete on a galaxy. Once the stellar mass exceeds  $\sim 10^7 M_{\odot}$ , the fraction becomes  $\lesssim 0.01$ . Considering the sensitivities of current telescopes, only massive galaxies with  $M_{\text{star}} \gtrsim 10^7 M_{\odot}$  have been observed. Therefore, population II stars mainly form in the observed candidate galaxies at  $z \gtrsim 10$ . We find that the mass fraction is insensitive to the redshift in the range of  $z = 10 - 20$ . Given that the metal production source is only type-II supernovae, the total metal mass released is simply proportional to the stellar mass. Thus, the insensitive redshift dependence indicates similar metal mixing with the in-

terstellar gas in the redshift range. Our simulations suggest that low-mass galaxies with  $M_{\text{star}} \lesssim 10^5 M_{\odot}$  host population III stars with non-negligible fraction  $\gtrsim 0.1$ . Recently, [Riaz et al. \(2022\)](#) showed the mass fraction of Pop III stars to the total stellar masses based on their semi-numerical models ([Hartwig et al. 2022](#)). The mass fraction of low-mass galaxies with  $M_{\text{star}} \sim 10^{4-5} M_{\odot}$  is similar to their results. On the other hand, our results for massive galaxies are much higher. Our cosmological simulations indicate that the gas in mini-haloes can survive as the primordial state and contribute to the Pop III star formation in massive galaxies.

A lower panel of figure 5 represents the contribution of Pop III stars to the UV flux at  $\lambda = 1500 \text{ \AA}$  in a rest frame. The contribution fraction also decreases with the mass of Pop III stars. However, since the mass-to-light ratio of Pop III stars is large and their effective temperature is high  $T \sim 10^5 \text{ K}$  ([Schaerer 2002](#)), the contribution is moderately large even if the mass fraction of Pop III stars is low. In the cases of  $M_{\text{star}} \sim 10^7 M_{\odot}$ , it can be a few percent. Therefore, a part of the observed fluxes by JWST could be contributed by PopIII stars. The UV flux can be dominated by Pop III stars if the stellar mass is lower than  $\sim 10^5 M_{\odot}$ . However, the low-mass systems are likely to be too faint for the sensitivities of current telescopes. Therefore, next-generation telescopes or gravitationally lensed galaxies by foreground sources might be required for direct observations of population III star clusters. Very recently, [Vanzella et al. \(2023\)](#) indicated a candidate of a Pop III star cluster with the mass of  $\lesssim 10^4 M_{\odot}$  with the gravitational lens effect. The total metallicity even for low-mass galaxies with  $M_{\text{star}} \lesssim 10^5 M_{\odot}$  exceed  $\sim 10^{-3} Z/Z_{\odot}$ . Therefore, the formation of population III stars indicates inhomogeneous metal enrichment in a galaxy. The formation sites of population III stars are somewhat far from the high-density regions of population II stars where the metal enrichment proceeds earlier. Also, we find that the number fraction of galaxies hosting young Pop III stars increases from  $\sim 0.3$  for  $M_{\text{star}} = 10^5 M_{\odot}$  to  $\sim 0.7$  for  $M_{\text{star}} = 10^8 M_{\odot}$ . The low-mass galaxies without young Pop III stars consist of two states, star-forming only with Pop II stars or quenching of star formation due to the SN feedback. Massive haloes are likely to distribute near the centre of overdense regions and primordial gas hosted by mini-haloes can accrete them frequently. Therefore, the massive haloes can host young Pop III stars although the mass fraction is low.

Note that, even for the population III stars, we model the star formation by replacing a gas particle with a stellar particle with the uniform mass  $\sim 8 \times 10^3 M_{\odot}$ , which models a star cluster. Therefore, the stellar particles release the same SN energy and metal mass. However, if the total stellar mass is smaller than  $\sim 10^3 M_{\odot}$  in low-mass haloes, the IMF may not be universal, resulting in unequal SN feedback and metal amount ([Abe et al. 2021](#)). This can enhance spatial fluctuation of metal distribution in the large cosmic volume. Therefore, the metal distributions in low-mass galaxies are likely to change with the resolution and the model of population III stars. We will investigate these impacts on the fraction of population III stars in future work.

Here, we derive intrinsic SEDs of galaxies by using a stellar synthesis code STARBURST99 ([Leitherer et al. 1999](#)). Figure 6 shows the SEDs of the most massive progenitors at  $z = 12, 14, 17,$  and  $20$ . In this work, we estimate SEDs with the optically-thin approximation, i.e., no dust attenuation,

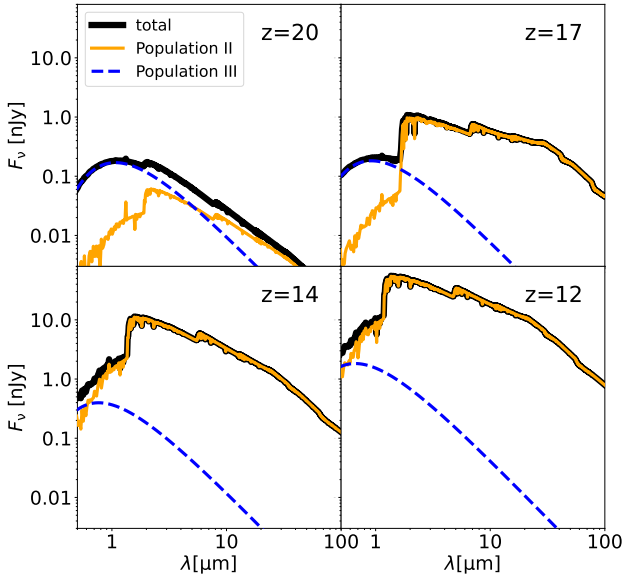


**Figure 6.** SEDs of the most massive progenitors at  $z = 12, 14, 17,$  and  $20$ . Blue dashed and orange solid lines show the radiation only from population III and II stars, respectively. Black solid lines are SEDs considering both stellar populations.

which can be reasonable for low-mass and low-metallicity galaxies (Yajima et al. 2012, 2014; Cullen et al. 2017). The observed blue UV-slope ( $\beta \lesssim -2$ ) supports the assumption (Furtak et al. 2023; Naidu et al. 2022). The contribution from population III stars is estimated with the assumption of the brightness temperature of  $10^5$  K and the mass-to-luminosity ratio for  $120 M_{\odot}$  derived in Schaerer (2002). The mass fractions of Pop III stars of the galaxies are  $1.1 \times 10^{-3}, 1.8 \times 10^{-3}, 4.7 \times 10^{-3},$  and  $0.2$  at  $z = 12, 14, 17,$  and  $20$ , respectively. Their contributions to UV luminosity densities at  $\lambda = 1500 \text{ \AA}$  are  $1.4 \times 10^{-2}, 1.6 \times 10^{-2}, 7.5 \times 10^{-2}$  and  $0.57$ . We find that the contribution fraction can be fit by  $\log_{10} f_{\text{UV, Pop III}} = 0.66 \log_{10} \left( \frac{M_{\text{star, Pop III}}}{M_{\text{star}}} \right) + 0.20$ . At  $z = 20$ , the light from Pop III stars dominates at UV wavelengths. At the lower redshifts, the UV continuum fluxes are dominated by Pop II stars. We measure the UV slopes of the SEDs by using the flux densities at  $\lambda = 1300, 2000,$  and  $3000 \text{ \AA}$ . It shows  $\beta = -2.68, -2.76, -2.62$  and  $-3.33$  at  $z = 12, 14, 17$  and  $20$ , respectively. These naturally reproduce the very blue slopes of the observed galaxies (Atek et al. 2022; Furtak et al. 2023). Note that, we do not consider the nebular emission in the above SEDs. If the nebular continuum at the UV wavelengths is added into the SEDs, the slopes are changed to  $\beta = -2.55, -2.60, -2.57$  and  $-2.98$  at  $z = 12, 14, 17$  and  $20$ . Furthermore, dust extinction can make the SEDs redder at lower redshifts.

The galaxies at  $z \leq 14$  have UV flux densities of  $\gtrsim 10$  nJy that are observable by JWST with a reasonable integration time. We suggest that a part of the observed fluxes of candidate galaxies at  $z \gtrsim 10$  could be contributed by Pop III stars. If the sensitivity of future observations at  $3 \mu\text{m}$  will

reach  $\sim 0.1$  nJy, the UV light dominated by Pop III stars can be observed directly. Also, note that Lyman continuum fluxes can be dominated by Pop III stars significantly even if the mass fraction of Pop III stars is low  $\lesssim 0.1$ . For example, the contribution of Pop III stars to the LyC flux at  $900 \text{ \AA}$  for the galaxy at  $z = 17$  is  $0.7$ . Thus, these galaxies consisting of both Pop II and III stars can be strong ionizing sources. In addition, they may have unique properties in SEDs with high equivalent widths of doubly ionized oxygen, carbon, and helium (see also, Nakajima & Maiolino 2022). In this work, we do not take into account the radiative transfer in the galaxies. However, since the galaxies are low-mass and low-metallicity systems, non-ionizing UV continuum photons are expected to escape efficiently. Therefore, the estimated UV-slopes are unlikely to change significantly. On the other hand, the escape fraction of LyC photons can change with time depending on the inhomogeneous gas structure due to the SN feedback (Yajima et al. 2014; Paardekooper et al. 2015; Kimm et al. 2015; Trebitsch et al. 2017). In the case of a high escape fraction, HeII and other metal lines can be faint. As shown in Ono et al. (2022), the sizes of our modelled galaxies change with time significantly. In phases when dusty gas compactly distributes star-forming regions at the galactic center, UV photons can be attenuated even at such high redshifts. In practice, the gas at the galactic center reaches a metallicity with  $Z \gtrsim 0.1 Z_{\odot}$  at  $z \sim 10$  (see also, Isobe et al. 2023b). The escape fraction of photons sensitively depends on the covering fraction of dusty gas clouds from young stars. We will perform radiative transfer simulations in future work.

#### 4 DISCUSSION & SUMMARY

We have investigated the star formation and physical properties in the first galaxies formed in overdense regions modelled by the FOREVER22 simulation project. Our simulations followed the evolution from mini-haloes hosting Pop III stars to massive galaxies with  $M_{\text{h}} > 10^{11} M_{\odot}$ . Our findings are summarized as follows.

- SFR increases with the halo mass and changes in the short-time period due to the supernova feedback. Once the halo mass exceeds  $\sim 10^{11} M_{\odot}$ , galaxies continuously form stars with  $\text{SFR} \gtrsim 10 M_{\odot} \text{ yr}^{-1}$  and induce starbursts with  $\sim 100 M_{\odot} \text{ yr}^{-1}$ . Even massive galaxies in overdense regions cannot reproduce the observed stellar masses and SFRs of candidate galaxies at  $z \sim 16$  suggested by Donnan et al. (2023), Harikane et al. (2023) and Naidu et al. (2022).

- Our simulations reproduce the relation between  $M_{\text{UV}}$  and  $M_{\text{star}}$  of the observed galaxies at  $z \gtrsim 10$  nicely. The galaxies with  $M_{\text{star}} \gtrsim 10^8 M_{\odot}$  show UV brightness of  $\lesssim -18$  mag which is observable by JWST.

- Even when the galaxy is metal enriched and forms Pop II stars, Pop III stars can form in zero-metallicity spots. The mass fraction of Pop III stars decreases as the stellar mass increases, and it is  $< 0.01$  for galaxies with  $M_{\text{star}} \sim 10^7 M_{\odot}$ . Therefore, candidate galaxies at  $z \gtrsim 10$  by JWST can be dominated by Pop II stars. We suggest that a part of galaxies with  $M_{\text{star}} \lesssim 10^5 M_{\odot}$  can host Pop III stars with a non-negligible fraction  $\gtrsim 0.1$ .

- We model SEDs of galaxies with Pop II and Pop III stars. The UV continuum fluxes of massive galaxies at  $z \leq 17$  are dominated by Pop II stars. However, a few percent of

UV fluxes can be from Pop III stars because of their large mass-to-luminosity ratio. The galaxies at  $z \leq 14$  have the brightness of  $\gtrsim 10$  nJy at  $\lambda = 2 \mu\text{m}$  which can be observable by JWST with a reasonable integration time.

The estimated physical properties and redshifts of the observed galaxies at  $z \gtrsim 10$  are not robust. Future spectroscopic observations would present more reliable data and constrain the physical properties of galaxies. On the other hand, the physical properties of first galaxies modelled by numerical simulations can depend on the resolution and the models of star formation and feedback (Abe et al. 2021). Also, the seeding of the first massive black holes is still under debate (Inayoshi et al. 2020), and it may change the physical properties of galaxies and SEDs. The star formation efficiency of massive haloes with  $M_{\text{h}} \gtrsim 10^{10} M_{\odot}$  at  $z \sim 10$  is similar to the results in Behroozi et al. (2020) and somewhat higher than Kannan et al. (2022a). In this paper, we newly provide insights about the relationship between Pop III stars and massive galaxies at  $z \gtrsim 10$ . The physical properties are likely to sensitively depend on the resolution, the star formation, and the feedback models. We will investigate the model and resolution dependencies on the first galaxy formation in future work.

## ACKNOWLEDGMENTS

The numerical simulations were performed on the computer cluster, XC50 in NAOJ, and Trinity at Center for Computational Sciences in University of Tsukuba. This work is supported in part by MEXT/JSPS KAKENHI Grant Number 17H04827, 20H04724, 21H04489 (HY), 20K22358, 22H01258 (TH), NAOJ ALMA Scientific Research Grant Numbers 2019-11A, JST FOREST Program, Grant Number JP-MJFR202Z, and Astro Biology Center Project research AB041008 (HY). For the purpose of open access, the author has applied a Creative Commons Attribution (CC BY) licence to any Author Accepted Manuscript version arising from this submission.

## DATA AVAILABILITY

The data underlying this article will be shared on reasonable request to the corresponding author.

## REFERENCES

Abe M., Yajima H., Khochfar S., Dalla Vecchia C., Omukai K., 2021, *MNRAS*, **508**, 3226  
 Agarwal B., Dalla Vecchia C., Johnson J. L., Khochfar S., Paardekooper J.-P., 2014, *MNRAS*, **443**, 648  
 Arata S., Yajima H., Nagamine K., Li Y., Khochfar S., 2019, *MNRAS*, **488**, 2629  
 Arrabal Haro P., et al., 2023, *arXiv e-prints*, p. [arXiv:2303.15431](#)  
 Atek H., et al., 2022, *arXiv e-prints*, p. [arXiv:2207.12338](#)  
 Bakx T. J. L. C., et al., 2022, *arXiv e-prints*, p. [arXiv:2208.13642](#)  
 Behroozi P., Wechsler R. H., Hearin A. P., Conroy C., 2019, *MNRAS*, **488**, 3143  
 Behroozi P., et al., 2020, *MNRAS*, **499**, 5702  
 Bouwens R. J., Stefanon M., Oesch P. A., Illingworth G. D., Nanayakkara T., Roberts-Borsani G., Labbé I., Smit R., 2019, *ApJ*, **880**, 25

Bunker A. J., et al., 2023, *arXiv e-prints*, p. [arXiv:2302.07256](#)  
 Capak P. L., et al., 2015, *Nature*, **522**, 455  
 Chiaki G., Wise J. H., 2019, *MNRAS*, **482**, 3933  
 Chon S., Omukai K., Schneider R., 2021, *MNRAS*, **508**, 4175  
 Cullen F., McLure R. J., Khochfar S., Dunlop J. S., Dalla Vecchia C., 2017, *MNRAS*, **470**, 3006  
 Cullen F., et al., 2022, *arXiv e-prints*, p. [arXiv:2208.04914](#)  
 Dalla Vecchia C., Schaye J., 2012, *MNRAS*, **426**, 140  
 Dekel A., Cox T. J., 2006, *MNRAS*, **370**, 1445  
 Donnan C. T., et al., 2023, *MNRAS*, **518**, 6011  
 Ferland G. J., 2000, in Arthur S. J., Brickhouse N. S., Franco J., eds, *Revista Mexicana de Astronomia y Astrofisica Conference Series Vol. 9, Revista Mexicana de Astronomia y Astrofisica Conference Series*. pp 153–157  
 Finkelstein S. L., et al., 2013, *Nature*, **502**, 524  
 Finkelstein S. L., et al., 2023, *ApJ*, **946**, L13  
 Frebel A., Johnson J. L., Bromm V., 2007, *MNRAS*, **380**, L40  
 Freedman W. L., 2021, *ApJ*, **919**, 16  
 Furtak L. J., Shuntov M., Atek H., Zitrin A., Richard J., Lehnert M. D., Chevallard J., 2023, *MNRAS*, **519**, 3064  
 Gabrielpillai A., Somerville R. S., Genel S., Rodriguez-Gomez V., Pandya V., Yung L. Y. A., Hernquist L., 2022, *MNRAS*, **517**, 6091  
 Harikane Y., et al., 2023, *ApJS*, **265**, 5  
 Hartwig T., et al., 2022, *ApJ*, **936**, 45  
 Hashimoto T., et al., 2018, *Nature*, **557**, 392  
 Hirano S., Hosokawa T., Yoshida N., Omukai K., Yorke H. W., 2015, *MNRAS*, **448**, 568  
 Inayoshi K., Visbal E., Haiman Z., 2020, *ARA&A*, **58**, 27  
 Inayoshi K., Harikane Y., Inoue A. K., Li W., Ho L. C., 2022, *arXiv e-prints*, p. [arXiv:2208.06872](#)  
 Inoue A. K., et al., 2016, *Science*, **352**, 1559  
 Jeon M., Bromm V., 2019, *MNRAS*, **485**, 5939  
 Jiang L., et al., 2021, *Nature Astronomy*, **5**, 256  
 Johnson J. L., Dalla V. C., Khochfar S., 2013, *MNRAS*, **428**, 1857  
 Kannan R., et al., 2022a, *arXiv e-prints*, p. [arXiv:2210.10066](#)  
 Kannan R., Garaldi E., Smith A., Pakmor R., Springel V., Vogelsberger M., Hernquist L., 2022b, *MNRAS*, **511**, 4005  
 Kimm T., Cen R., Rosdahl J., Yi S., 2015, preprint, ([arXiv:1510.05671](#))  
 Komatsu E., et al., 2011, *ApJS*, **192**, 18  
 Latif M. A., Whalen D. J., Khochfar S., Herrington N. P., Woods T. E., 2022a, *Nature*, **607**, 48  
 Latif M. A., Whalen D., Khochfar S., 2022b, *ApJ*, **925**, 28  
 Leitherer C., et al., 1999, *ApJS*, **123**, 3  
 Liu B., Bromm V., 2020, *MNRAS*, **497**, 2839  
 Lovell C. C., Vijayan A. P., Thomas P. A., Wilkins S. M., Barnes D. J., Irodoto D., Roper W., 2021, *MNRAS*, **500**, 2127  
 Ma X., Quataert E., Wetzel A., Hopkins P. F., Faucher-Giguère C.-A., Kereš D., 2020, *MNRAS*, **498**, 2001  
 Maio U., Ciardi B., Dolag K., Tornatore L., Khochfar S., 2010, *MNRAS*, **407**, 1003  
 Maio U., Khochfar S., Johnson J. L., Ciardi B., 2011, *MNRAS*, **414**, 1145  
 Naidu R. P., et al., 2022, *ApJ*, **940**, L14  
 Nakajima K., Maiolino R., 2022, *MNRAS*, **513**, 5134  
 Ocvirk P., et al., 2016, *MNRAS*, **463**, 1462  
 Oesch P. A., et al., 2013, *ApJ*, **773**, 75  
 Oesch P. A., et al., 2016, *ApJ*, **819**, 129  
 Omukai K., Tsuribe T., Schneider R., Ferrara A., 2005, *ApJ*, **626**, 627  
 Ono Y., et al., 2012, *ApJ*, **744**, 83  
 Ono Y., et al., 2022, *arXiv e-prints*, p. [arXiv:2208.13582](#)  
 Ouchi M., et al., 2018, *PASJ*, **70**, S13  
 Paardekooper J.-P., Khochfar S., Dalla Vecchia C., 2013, *MNRAS*, **429**, L94  
 Paardekooper J.-P., Khochfar S., Dalla Vecchia C., 2015, *MNRAS*, **451**, 2544

- Pakmor R., et al., 2022, [arXiv e-prints](#), p. [arXiv:2210.10060](#)
- Pallottini A., Ferrara A., Gallerani S., Salvadori S., D’Odorico V., 2014, [MNRAS](#), **440**, 2498
- Planck Collaboration et al., 2020, [A&A](#), **641**, A6
- Popping G., 2022, [arXiv e-prints](#), p. [arXiv:2208.13072](#)
- Regan J. A., Haehnelt M. G., 2009, [MNRAS](#), **396**, 343
- Riaz S., Hartwig T., Latif M. A., 2022, [ApJ](#), **937**, L6
- Rosdahl J., et al., 2022, [MNRAS](#), **515**, 2386
- Schaerer D., 2002, [A&A](#), **382**, 28
- Schaerer D., de Barros S., 2009, [A&A](#), **502**, 423
- Schaye J., Dalla Vecchia C., 2008, [MNRAS](#), **383**, 1210
- Schaye J., et al., 2010, [MNRAS](#), **402**, 1536
- Schaye J., et al., 2015, [MNRAS](#), **446**, 521
- Shang C., Bryan G. L., Haiman Z., 2010, [MNRAS](#), **402**, 1249
- Shibuya T., Kashikawa N., Ota K., Iye M., Ouchi M., Furusawa H., Shimasaku K., Hattori T., 2012, [ApJ](#), **752**, 114
- Smith B. D., Wise J. H., O’Shea B. W., Norman M. L., Khochfar S., 2015, [MNRAS](#), **452**, 2822
- Song M., Finkelstein S. L., Livermore R. C., Capak P. L., Dickinson M., Fontana A., 2016, [ApJ](#), **826**, 113
- Springel V., 2005, [MNRAS](#), **364**, 1105
- Stacy A., Bromm V., 2014, [ApJ](#), **785**, 73
- Sugimura K., Matsumoto T., Hosokawa T., Hirano S., Omukai K., 2020, [ApJ](#), **892**, L14
- Susa H., Hasegawa K., Tominaga N., 2014, [ApJ](#), **792**, 32
- Tamura Y., et al., 2019, [ApJ](#), **874**, 27
- Topping M. W., Stark D. P., Endsley R., Plat A., Whittler L., Chen Z., Charlot S., 2022, [arXiv e-prints](#), p. [arXiv:2208.01610](#)
- Tornatore L., Ferrara A., Schneider R., 2007, [MNRAS](#), **382**, 945
- Trebtsch M., Blaizot J., Rosdahl J., Devriendt J., Slyz A., 2017, [MNRAS](#), **470**, 224
- Vanzella E., et al., 2023, [arXiv e-prints](#), p. [arXiv:2305.14413](#)
- Wise J. H., Turk M. J., Norman M. L., Abel T., 2012, [ApJ](#), **745**, 50
- Wise J. H., Demchenko V. G., Halicek M. T., Norman M. L., Turk M. J., Abel T., Smith B. D., 2014, [MNRAS](#), **442**, 2560
- Wise J. H., Regan J. A., O’Shea B. W., Norman M. L., Downes T. P., Xu H., 2019, [Nature](#), **566**, 85
- Wolcott-Green J., Haiman Z., Bryan G. L., 2011, [MNRAS](#), **418**, 838
- Wollenberg K. M. J., Glover S. C. O., Clark P. C., Klessen R. S., 2020, [MNRAS](#), **494**, 1871
- Xu H., Norman M. L., O’Shea B. W., Wise J. H., 2016, [ApJ](#), **823**, 140
- Yajima H., Khochfar S., 2016, [MNRAS](#), **457**, 2423
- Yajima H., Umemura M., Mori M., Nakamoto T., 2009, [MNRAS](#), **398**, 715
- Yajima H., Choi J.-H., Nagamine K., 2011, [MNRAS](#), **412**, 411
- Yajima H., Li Y., Zhu Q., Abel T., 2012, [MNRAS](#), **424**, 884
- Yajima H., Li Y., Zhu Q., Abel T., Gronwall C., Ciardullo R., 2014, [MNRAS](#), **440**, 776
- Yajima H., Nagamine K., Zhu Q., Khochfar S., Dalla Vecchia C., 2017, [ApJ](#), **846**, 30
- Yajima H., Sugimura K., Hasegawa K., 2018, [MNRAS](#), **477**, 5406
- Yajima H., et al., 2022, [MNRAS](#), **509**, 4037
- Yoon I., et al., 2022, [arXiv e-prints](#), p. [arXiv:2210.08413](#)